Atmospheric
Chemistry
and Physics

Supplement of

Measuring and modeling investigation of the net photochemical ozone production rate via an improved dual-channel reaction chamber technique

Yixin Hao et al.

Correspondence to: Jun Zhou (junzhou@jnu.edu.cn) and Bin Yuan (byuan@jnu.edu.cn)

1   **S1: The reaction and reference chambers.**

2   **1.1 Schematic diagram**

3   The specifications of the reaction and reference chambers are basically the same, which are composed of

4   a quartz glass cylinder, two O rings, two PTFE plates, and PTFE joint connections. Both inlet and outlet

5   of the quartz cylinder are connected to the PTFE plates and sealed by the O rings, the PTFE plates were

6   then fixed by the stainless-steel plates on a stainless-steel shelf. The length and inner diameter of the

7   quartz glass cylinder are 700 mm and 190.5 mm, respectively. The PTFE plate has a PTFE tube (outer

8   diameter of 12.7 mm) for air intake and outflow. For air inject, an PTFE tube passes through one PTFE

9   plate and is bent as "L-shape" at the inner surface side of the PTFE plate. The other PTFE plate on the

10   other side is equipped with a straight PTFE tube for air outflow (see Fig. S1).
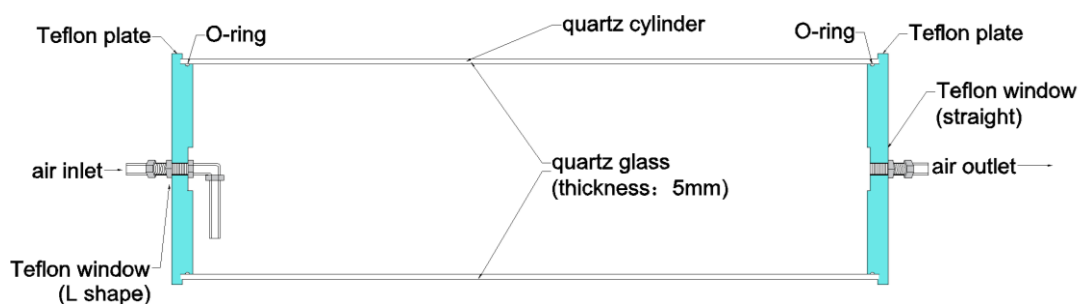
11

12   **Figure S1: Schematic diagram of the reaction and reference chambers.**

13   **1.2 Residence time of air in the reaction and reference chambers**

14   The residence time of air in the two chambers ($\langle\tau\rangle$) are critical for calculating $P(O_3)_{net}$. The air flow rate

15   through the reaction and reference chambers can be set at 1.3, 2, 3, 4, and 5 L min^{-1}, respectively,

16   depending on the measurement environment, therefore the residence time of air in these two chambers

17   under different air flow rates were also varied. The experimental schematic diagram and results of other

18   air flow rates are shown in the Supplement (Figs. S2 and S3).

19   We first measured $\langle\tau\rangle$ by introducing a short pulse of NO_2 gas at 5 L min^{-1} (obtained by mixing 0.2

20   L min^{-1} of 2.08 ppmv NO_2 standard gas with 5.2 L min^{-1} ultrapure) into the reaction and reference

21   chambers at $\tau = 0$, the airflow rates in the reaction and reference chambers were controlled by the flow

22   rate of the CAPS-NO_2 monitor (1.11 L min^{-1}) and pump (3.89 L min^{-1}), the time profile of NO_2 mixing

23   ratios ($C(\tau)$) at the exit of the chamber was measured using the CAPS-NO_2 monitor. The pulse width of

24 the introduced NO_2 gas was approximately 20 s and sufficiently shorter than $\langle\tau\rangle$. $C(\tau)$ is normalized by

25 Eq. (S1), which converts $C(\tau)$ to a probability density function ($E(\tau)$) (Sadanaga et al., 2017).

26 $E\langle\tau\rangle = \dfrac{C(\tau)}{\int_0^\infty C(\tau)\,d\tau}$ (S1)

27 $\langle\tau\rangle$ is an expectation value and was calculated using Eq. (S2).

28 $\langle\tau\rangle = \int_0^\infty \tau E\langle\tau\rangle d\tau = \int_0^\infty \dfrac{\tau C(\tau)}{\int_0^\infty C(\tau)\,d\tau}\,d\tau$ (S2)

29   Three sets of experiments of $\langle\tau\rangle$ of NO_2 in the reaction and reference chambers were carried out,

30 and the average $\langle\tau\rangle$ of NO_2 in the reaction and reference chambers were both 0.063 h, indicating that

31 there was no difference in the average $\langle\tau\rangle$ of the sampled air in these two chambers. We also investigated

32 $\langle\tau\rangle$ of NO_2 at the flow rate of 1.3, 2, 3, and 4 L min^{-1}, the measured average $\langle\tau\rangle$ were all closed to the

33 theoretical values. Figure S2 shows the schematic diagram of the experiments. We described the results

34 at the flow rates of 1.3, 2, 3, 4, and 5 L min^{-1} in Fig. S3 and Table S1.
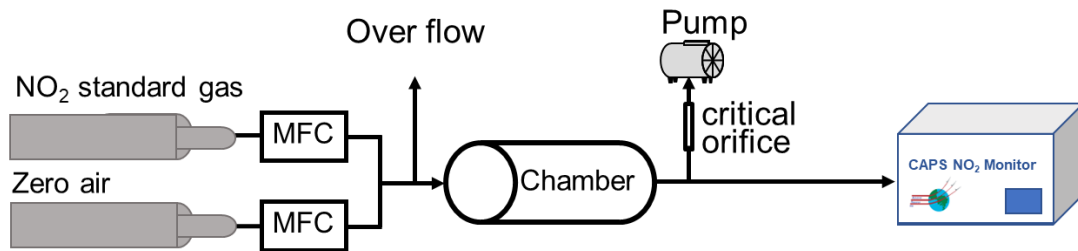
35

36 **Figure S2: Schematic diagram for measuring average residence time (MFC: Mass Flow Controller).**

37

38

39
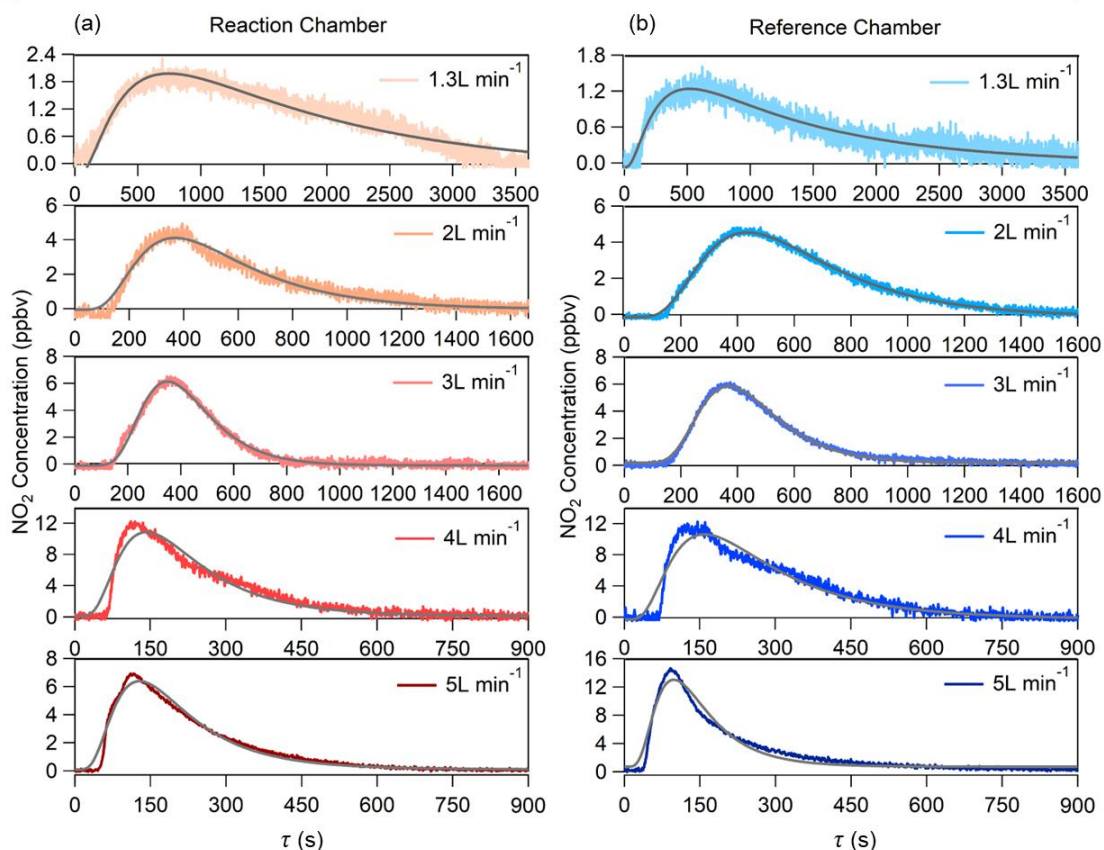
Figure S3: Average E(τ) time profiles in (a) the reaction and (b) the reference chambers at the sampling flow rates of 1.3, 2, 3, 4, and 5 L min^{-1}, respectively. The related residence time of NO$_2$ in the reaction and reference chambers of each air flow rate is shown in Table S1.

Table S1. Average residence time of air in the reaction and reference chambers.

Flow rate of air (L min^{-1})	Average residence time (h)	
	Reaction chamber	Reference chamber
1.3	0.350±0.0020	0.321±0.0026
2	0.160±0.0015	0.164±0.0022
3	0.111±0.0004	0.142±0.0002
4	0.067±0.0003	0.074±0.0003
5	0.063±0.0007	0.063±0.0005

1.3 Wall losses of NO$_2$ and O$_3$ in the reaction and reference chambers

In order to investigate the wall loss of O$_3$ or NO$_2$, we injected several steams of O$_3$ or NO$_2$ with different mixing ratios into the reaction and reference chambers, and measured the O$_3$ or NO$_2$ mixing ratios at the

4

49 inlet and outlet of the chambers. The O_3 used here were generated by injecting the ultrapure air into an

50 O_3 generator (P/N 97-0067-02, Analytic Jena, USA), O_3 mixing ratios were measured by a 2B O_3 monitor

51 based on a dual-channel UV-absorption technique (Model 205, 2B Technology, USA), and NO_2 mixing

52 ratios was monitored by the CAPS-NO_2 monitor. The wall losses of O_3 and NO_2 can be calculated as:

53 $O_{3\,loss} = \left(1 - \frac{[O_3]_{out}}{[O_3]_{in}}\right) \times 100\ \%$ (S3)

54 $NO_{2\,loss} = \left(1 - \frac{[NO_2]_{out}}{[NO_2]_{in}}\right) \times 100\ \%$ (S4)

55 where $[O_3]_{out}$ and $[NO_2]_{out}$ represent the mixing ratio of gas passing through the reaction and reference

56 chambers, $[O_3]_{in}$ and $[NO_2]_{in}$ represent the mixing ratio of gas passing through then bypass.

57   The experiments were conducted under dark conditions, the experimental schematic diagram is

58 shown in Fig. S4, and the results at the air flow rate of 1.3, 2, 3, 4, and 5 L min^{-1} are shown in Figs. S5-

59 S6 and Tables S2-S5. From Figs. S5-S6, at the air flow rate of 5 L min^{-1}, wall losses of O_3 in the reaction

60 and reference chambers were found to be approximately 0 % and 0.7 %, respectively, wall losses of NO_2

61 were found to be approximately less than 1.0 % for both chambers, which were smaller than the wall loss

62 of Ox in previous studies (as shown in Table S6), this indicates the small effects of Ox loss to $P(O_3)_{net}$

63 measurements in our NPOPR detection system. To investigate the influence of different flow rates to the

64 Ox wall losses, we also tested the wall loss of O_x at flow rates of 1.3, 2, 3, and 4 L min^{-1}, respectively,

65 we found that with the increase of the flow rate, the Ox wall losses decreased, but even with the flow rate

66 of 1.3 L min^{-1}, the wall loses were still smaller than 4 % and 2 % in the reaction chamber and the reference

67 chambers, respectively, more details are shown in Table S2. At the air flow rates of 1.3, 2, 3, and 4 L min^{-}

68 ^{1}, the wall losses of O_3 in the reaction chamber were found to be approximately 2 %, 0 %, 0 %, and 0 %,

69 respectively, the wall losses of O_3 in the reference chamber was found to be approximately 2 %, 1 %,

70 1 %, and 0 %, respectively. While the wall losses of NO_2 in the reaction chamber at the air flow rates of

71 1.3, 2, 3, and 4 L min^{-1} were found to be approximately 4 %, 4 %, 2 %, and 0 %, respectively, the wall

72 losses of NO_2 in the reference chamber were found to be approximately 2 %, 1 %, 0 %, and 0 %,

73 respectively. The regression lines have non-zero intercepts but not significant. We added the regression

74 fittings without intercept, and compared the regression fitting results with and without intercept (as

75 shown in Figs. S5 and S6). We found that the O_3 and NO_2 wall losses were not much different (as shown

76 in Tables S2 and S3), and the wall loss affected by the fitting intercepts for NO_2 (at ambient mixing ratios

77 of 0-100 ppbv) and O_3 (at ambient mixing ratios of 0-200 ppbv) at the air flow rate of 5 L min^{-1} were all

5

78 below 4 % (as shown in Tables S4 and S5). We found that when the O_3 have negative intercepts, the O_3

79 wall losses are still below 4 %, which is not significant.

80 Sklaveniti et al. (2018) found that the wall loss of NO_2 is significantly less than that of O_3 at higher

81 humidity levels. However, in our O_3 photo-enhanced uptake experiments, the wall loss of O_3 was almost

82 unaffected by humidity at a flow rate of 5 L min^{-1}. We also tested the wall losses of NO_2 and O_3 in the

83 chamber at a 5 L min^{-1} flow rate at different humidities of 35-75 %, the detailed results are shown in Fig.

84 S7 and S8, which shows that the variation in humidity effected the wall loss of NO_2 and O_3 by 0.03-

85 0.12 % and 1.06-1.19 %, respectively, which is much smaller than the instrument detection error (which

86 is 2 % at ambient NO_2 mixing ratios of 0-100 ppb), thus we didn't count this interference during the data

87 analysis.

88
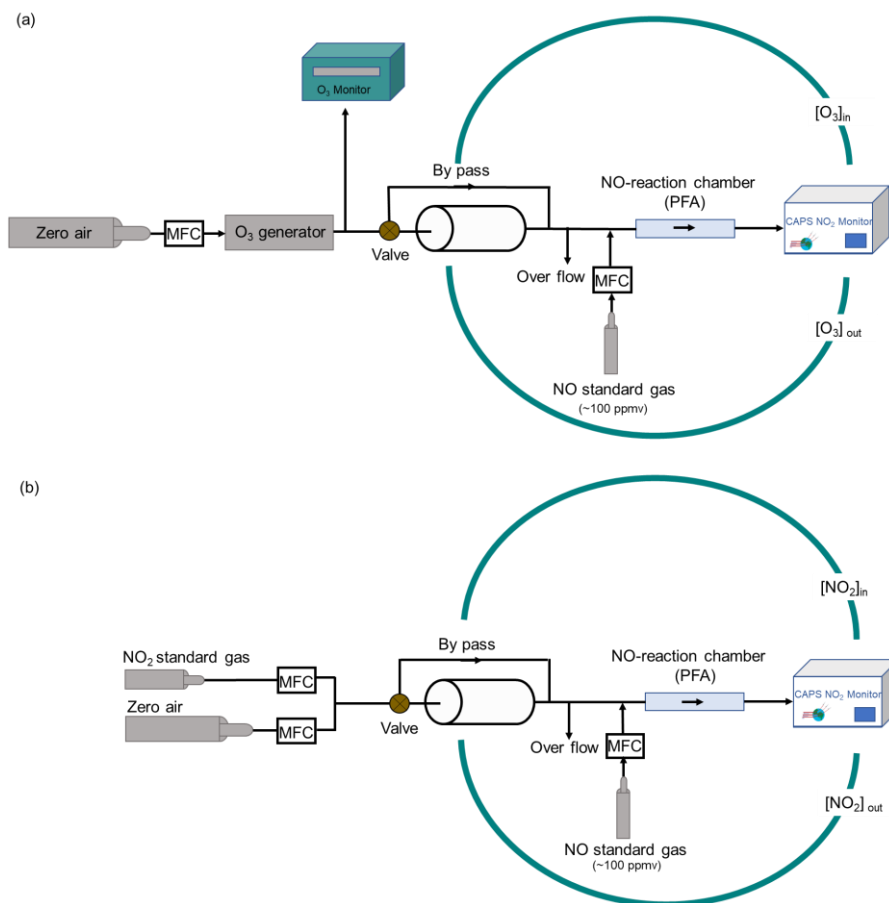
89
90
91 **Figure S4: Schematic diagram for testing (a) O_3 and (b) NO_2 wall loss in the reaction and reference chambers**
92 **(MFC: Mass Flow Controller).**
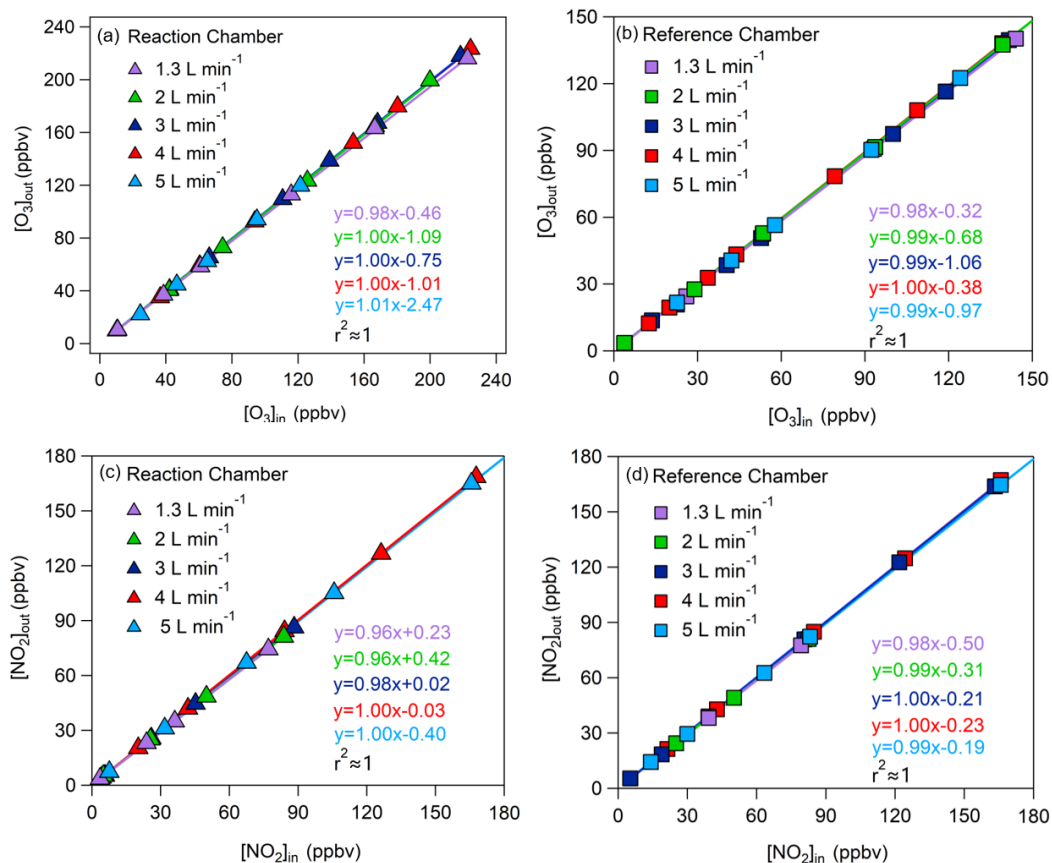
Figure S5: Relationship between (a,b) $[O_3]_{in}$ and $[O_3]_{out}$ and (c,d) $[NO_2]_{in}$ and $[NO_2]_{out}$ in the reaction and reference chambers with intercepts at the flow rates of 1.3, 2, 3, 4, and 5 L min^{-1}, respectively, the solid lines represent the linear fitting of the O_3 or NO_2 mixing ratios at the inlet and outlet of the chambers.

98
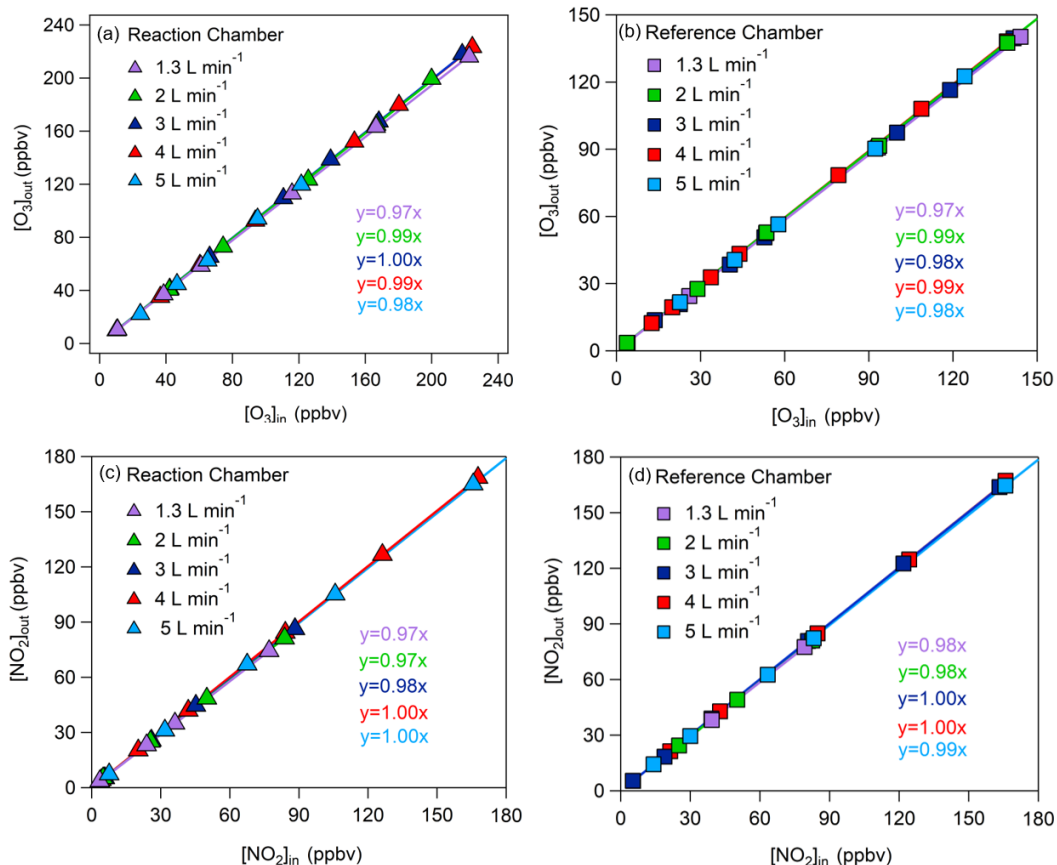
Figure S6: Relationship between (a, b) $[O_3]_{in}$ and $[O_3]_{out}$ and (c,d) $[NO_2]_{in}$ and $[NO_2]_{out}$ in the reaction and reference chambers without intercepts at the flow rates of 1.3, 2, 3, 4, and 5 L min^{-1}, respectively, the solid lines represent the linear fitting of the O_3 or NO_2 mixing ratios at the inlet and outlet of the chambers.

102

Table S2. Wall losses of O_3 and NO_2 of the reaction and reference chambers with intercepts.

Flow rate of air (L min^{-1})	Wall losses of O_3 (%)		Wall losses of NO_2 (%)	
	Reaction chamber	Reference chamber	Reaction chamber	Reference chamber
1.3	2.0	2.0	4.0	2.0
2	0.0	1.0	4.0	1.0
3	0.0	1.0	2.0	0.0
4	0.0	0.0	0.0	0.0
5	0	0.7	0.3	0.6

104

105

106

107

108 **Table S3. Wall losses of O_3 and NO_2 of the reaction and reference chambers without intercepts.**

Flow rate of air (L min^{-1})	Wall losses of O_3 (%)		Wall losses of NO_2 (%)	
	Reaction chamber	Reference chamber	Reaction chamber	Reference chamber
1.3	3.0	3.0	3.0	2.0
2	1.0	1.0	3.0	2.0
3	0.0	2.0	2.0	0.0
4	1.0	1.0	0.0	0.0
5	2.0	2.0	0.0	1.0

109

110 **Table S4. NO_2 wall loss affected by the intercept.**

Ambient NO_2 mixing ratios (ppbv)	Wall loss affected by the intercept (NO_2, %)	
	Reaction chamber	Reference chamber
20	2.0	2.0
40	1.0	1.5
60	0.7	1.3
80	0.5	1.2
100	0.4	1.2

111

112 **Table S5. O_3 wall loss affected by the intercept.**

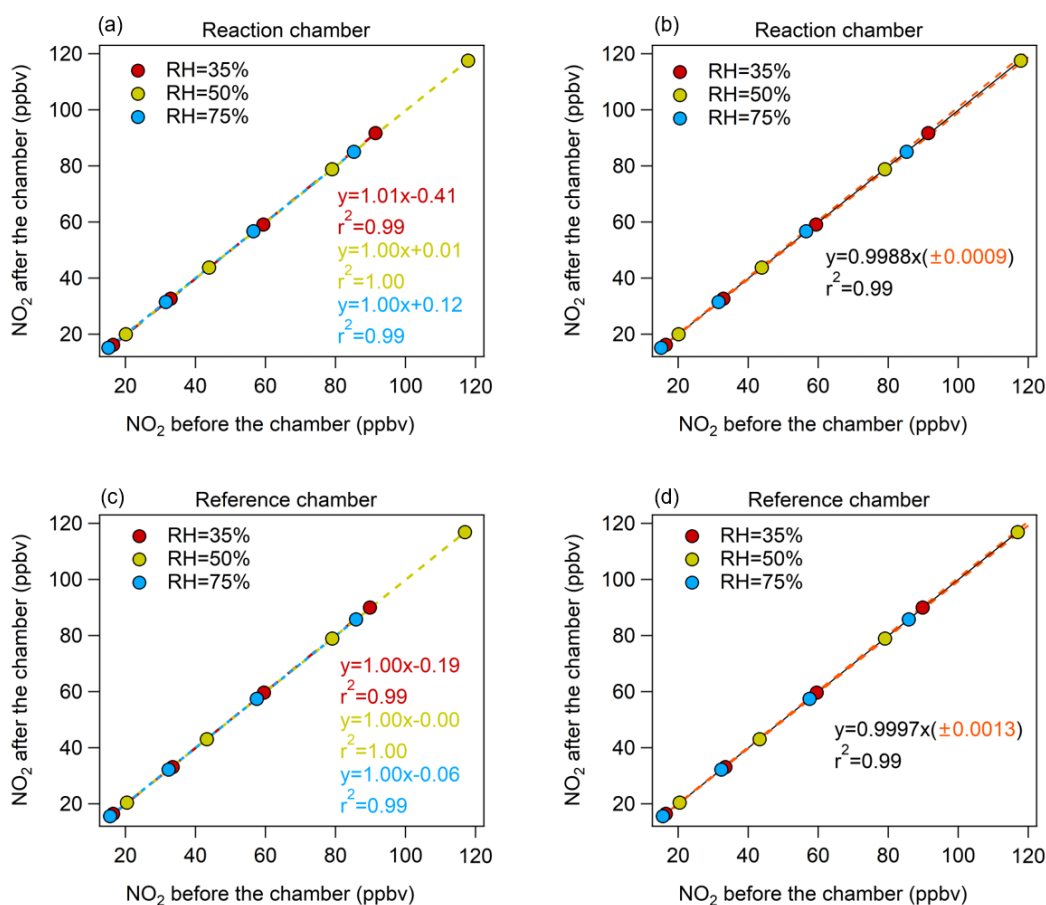| Ambient O_3 mixing ratios (ppbv)	Wall loss affected by the intercept (O_3, %)	
	Reaction chamber	Reference chamber
50	3.9	2.9
80	2.1	2.2
120	1.1	1.8
160	0.5	1.6
200	0.2	1.5

113

114

115

116

Table S6. O₃ and NO₂ wall loss from this study (at air flow rate of 5 L min^{-1}) and literatures (variable air flow rate).

|	Reaction chamber	Reference chamber	Literatures / air flow rate
O₃ loss rate	<3 %	<3 %	Cazorla *et al.*,2010 / 1.5 L min^{-1}
	1.3 %	1.4 %	Sadanaga *et al.*,2017 / 0.5 L min^{-1}
	5-15 %	5-13 %	Sklaveniti *et al.*, 2018 / 2.3 L min^{-1}
	0 %	0.7 %	This study / 5.0 L min^{-1}
NO₂ loss rate	<1 %	<1 %	Cazorla *et al.*,2010 / 1.5 L min^{-1}
	insignificant	insignificant	Sadanaga *et al.*,2017 / 0.5 L min^{-1}
	<3%	<3 %	Sklaveniti *et al.*, 2018 / 2.3 L min^{-1}
	0.3 %	0.6 %	This study / 5.0 L min^{-1}

Figure. S7 (a) and (c) represent the NO₂ wall loss at different humidities for the reaction and reference chambers, respectively, (b) and (d) represent the points fitted to all humidities, respectively. Uncertainty in the regression formula was one standard deviation (1σ).
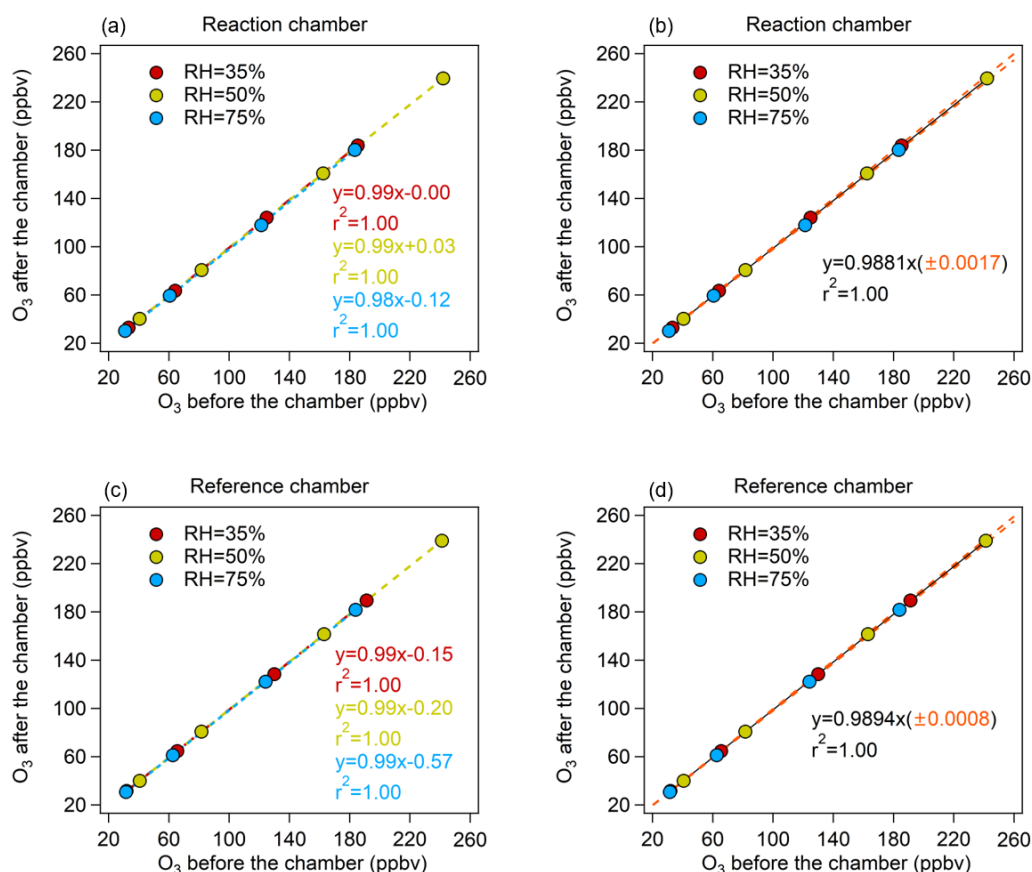
Figure. S8 (a) and (c) represent the O₃ wall loss at different humidities for the reaction and reference chambers, respectively, (b) and (d) represent the points fitted to all humidities, respectively. Uncertainty in the regression formula was one standard deviation (1σ).

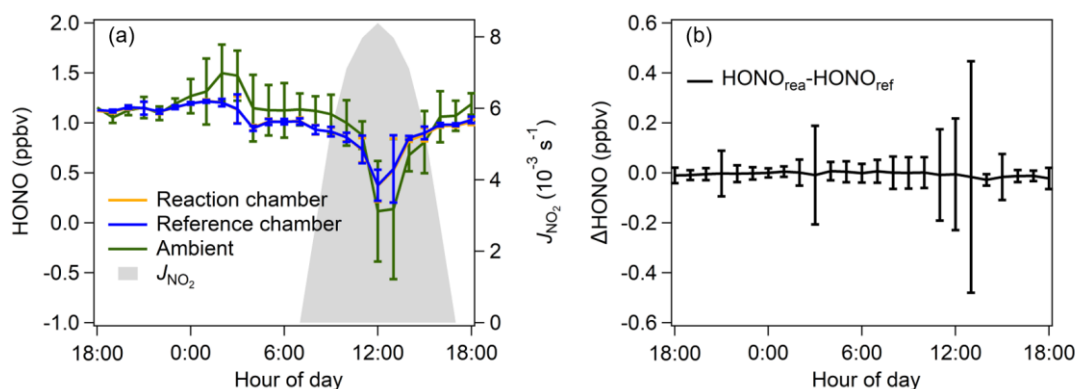## 1.4 HONO production in the reaction and reference chambers with variations of temperature and humidities

We tested the HONO production in the reaction and reference chambers under weather conditions similar to those during the SZMGT observations (humidities of 60-90% at a temperature of ~ 20 °C and $J(NO_2)$ of ~ 0-8 × 10⁻³ s⁻¹) at a 5 L min⁻¹ sampling flow rate. We found that the HONO mixing ratios in the reaction and reference chambers were almost the same and not statistically different from that in the ambient air within the standard deviation, as shown in Fig. S9; therefore, we assumed that the HONO production in the reaction and reference chambers would not cause a significant difference in $P(O_3)_{net}$ in the two chambers.

138

139 **Figure. S9 (a) The mixing ratios of HONO in the reaction and reference chambers and (b) the difference of**

140 **HONO mixing ratios the reaction and reference chambers.**

141 **1.5 The light transmittance in the reaction and reference chambers**

142 We measured the transmittivities of all species as follows: we simulated the illumination by adjusting

143 the sun light (SERIC XG-500B) to provide different intensities of illumination to study the solar UV

144 transmittance through the reaction and reference chambers. The photolysis frequencies of the species

145 NO_2, O_3, and HONO, etc. were measured using the Actinic flux spectrometer (PFS-100; Focused

146 Photonics Inc). Measurements are performed in laboratory. The UV blocking of the reference chamber

147 coated with UV protection film was evaluated by comparing the radiation measurements outside the

148 reference chamber with the measurements inside the reference chamber. Similar measurements and

149 comparisons were made for transparent reaction chambers. The results for the reaction and reference

150 chambers are shown in Table S7.

151 According to the working theory of the actinic flux spectrometer, the measurement error may rise

152 from the angular response deviation of the quartz receiver head. According to Bohn et al. (2017), the

153 measurement error of the actinic flux spectrometer can reach±5 %. According to this, we re-evaluated

154 the transmittivity error listed in Table 1 and Table S7 as follows:①calculate the absolute measurement

155 error of all measured J values inside and outside the reaction and reference chambers based on the ±5 %

156 instrument measurement error; ②calculate the average values of all the measured J values (including

157 ($J(NO_2)$, $J(O1D)$, $J(HONO)$, $J(H_2O_2)$, $J(NO_3\_M)$, $J(NO_3\_R)$, $J(HCHO\_M)$, and $J(HCHO\_R)$) inside and

158 outside the chambers; ③calculate the propagated error of transmittivity, using the following error

159 propagation equation:

12

160 $$\sigma_{Transmittivity}= \sqrt{(\frac{\sigma_{J\,value\,in}}{A_{J\,value\,in}})^2 + (\frac{\sigma_{J\,value\,out}}{A_{J\,value\,out}})^2} \tag{S5}$$

161 where $\sigma_{Transmittivity}$ represents the transmittivity error; $\sigma_{J\,value\,in}$ and $\sigma_{J\,value\,out}$ represent the

162 measurement error of J value inside and outside the chambers, respectively; $A_{J\,value\,in}$ and $A_{J\,value\,out}$

163 represent the average J values measured inside and outside the chambers, respectively.

164

165 **Table S7. Photolysis frequency J (s^{-1}) of different species and the transmittivities of J values in the reaction**

166 **and reference chambers. The normal and bold fonts correspond to the transmittivities of J values in the**

167 **reaction (clear) and reference (Ultem coated) chambers, respectively. The "transmittivities" column shows the**

168 **transmittivities of the tested species from the measurements conducted with the set photolysis frequencies**

169 **using SERIC XG-500B sunlight (this study) and ambient (literature). It should be noted that the errors listed**

170 **here are relatively large and may not reliable due to a limited number of measurement points (three points**

171 **for each species). The calculated transmittivity errors are 0.07 for all species based on the ±5 % measurement**

172 **error of the instrument.**

173

	Outside Chamber (s^{-1})	Inside chamber (s^{-1})	Transmittivities	
			Each experiment	Averaged
J(NO$_2$)	6.068E-03	5.744E-03	0.947	
	8.418E-03	8.598E-03	1.021	0.985 ±0.037
	1.360E-02	1.344E-02	0.988	
	5.996E-03	**4.700E-04**	**0.078**	
	1.064E-02	**1.134E-03**	**0.107**	**0.094 ±0.014**
	1.382E-02	**1.324E-03**	**0.095**	
J(O^{1}D)	5.609E-05	5.484E-05	0.978	
	1.088E-04	1.151E-04	1.050	1.020 ±0.04
	1.240E-04	1.240E-04	1.000	
	7.005E-05	**6.750E-07**	**0.010**	
	9.825E-05	**3.016E-06**	**0.031**	**0.019 ±0.011**
	1.243E-04	**2.205E-06**	**0.018**	
J(HONO)	1.058E-03	9.994E-04	0.944	
	1.468E-03	1.494E-03	1.018	0.983 ±0.037
	2.376E-03	2.344E-03	0.986	
	1.047E-03	**2.154E-06**	**0.002**	
	1.281E-03	**2.588E-06**	**0.002**	**0.002 ±0.0002**
	2.417E-03	**5.596E-06**	**0.002**	
J(H$_2$O$_2$)	6.157E-06	5.818E-06	0.944	1.000

|				
	1.370E-05	1.356E-05	0.990	±0.060
	1.200E-05	1.279E-05	1.065	
	6.145E-06	**3.451E-08**	**0.006**	**0.005**
	1.080E-05	**4.942E-08**	**0.005**	**±0.0006**
	1.393E-05	**6.160E-08**	**0.004**	
$J(NO_3\_M)$	1.314E-02	1.277E-02	0.971	1.002
	2.983E-02	2.993E-02	1.003	±0.030
	1.849E-02	1.906E-02	1.086	
	1.284E-02	**9.929E-03**	**0.773**	**0.916**
	2.342E-02	**2.437E-02**	**1.041**	**±0.134**
	3.040E-02	**2.839E-02**	**0.934**	
$J(NO_3\_R)$	9.881E-02	9.575E-02	0.970	0.999
	2.224E-01	2.226E-01	1.001	±0.030
	1.386E-01	1.425E-01	1.028	
	9.669E-02	**7.461E-02**	**0.772**	**0.913**
	1.751E-01	**1.814E-01**	**1.036**	**±0.030**
	2.268E-01	**2.113E-01**	**0.932**	
$J(HCHO\_M)$	2.645E-05	2.492E-05	0.942	0.997
	5.927E-05	5.845E-05	0.986	±0.006
	5.188E-05	5.514E-05	1.063	
	2.626E-05	**1.017E-07**	**0.0038**	**0.0015**
	4.643E-05	**1.810E-08**	**0.0004**	**±0.002**
	6.026E-05	**1.620E-08**	**0.0003**	
$J(HCHO\_R)$	5.800E-05	5.737E-05	0.989	1.021
	5.081E-05	5.394E-05	1.062	±0.004
	3.594E-05	3.617E-05	1.007	
	3.174E-05	**2.670E-09**	**~0**	**0.0026**
	4.561E-05	**1.800E-07**	**0.0039**	**±0.002**
	5.892E-05	**2.290E-07**	**0.0039**	

174
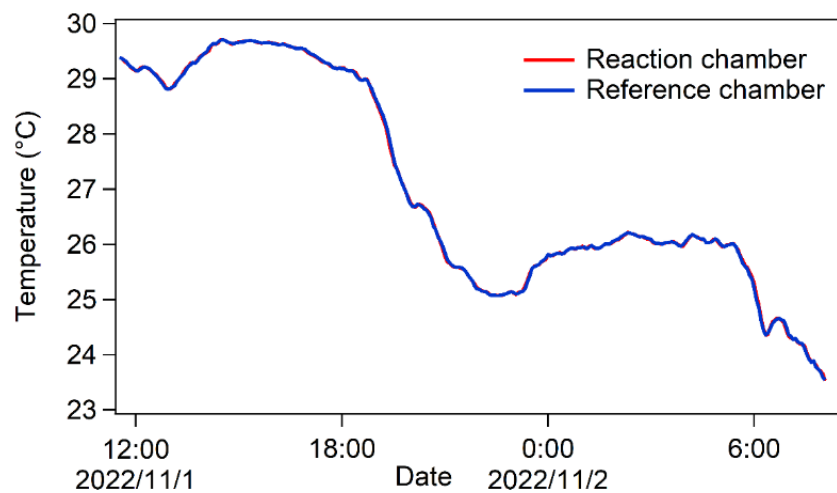
175
Figure S10. Air temperature in the reaction and reference chambers during the ambient field observation on
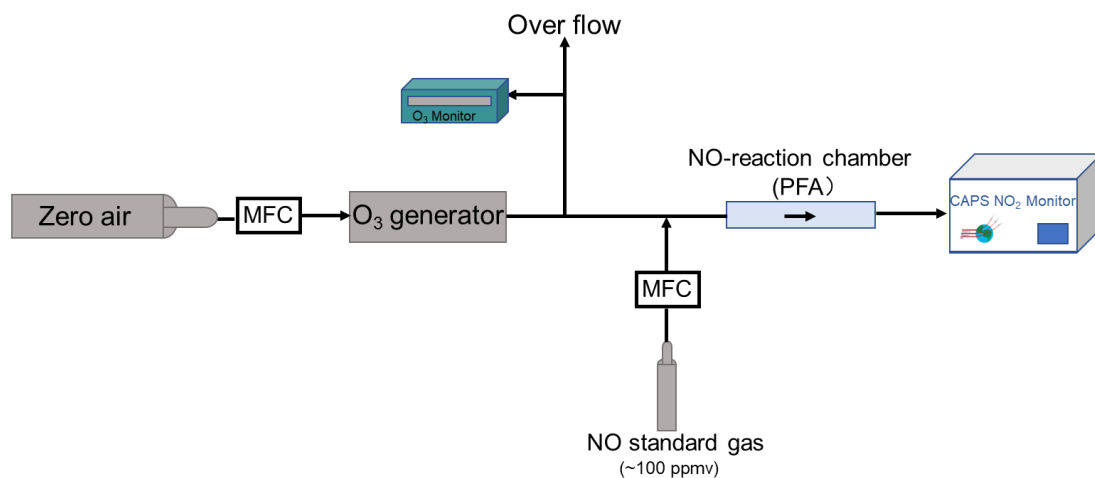Panyu campus of Jinan University.

178
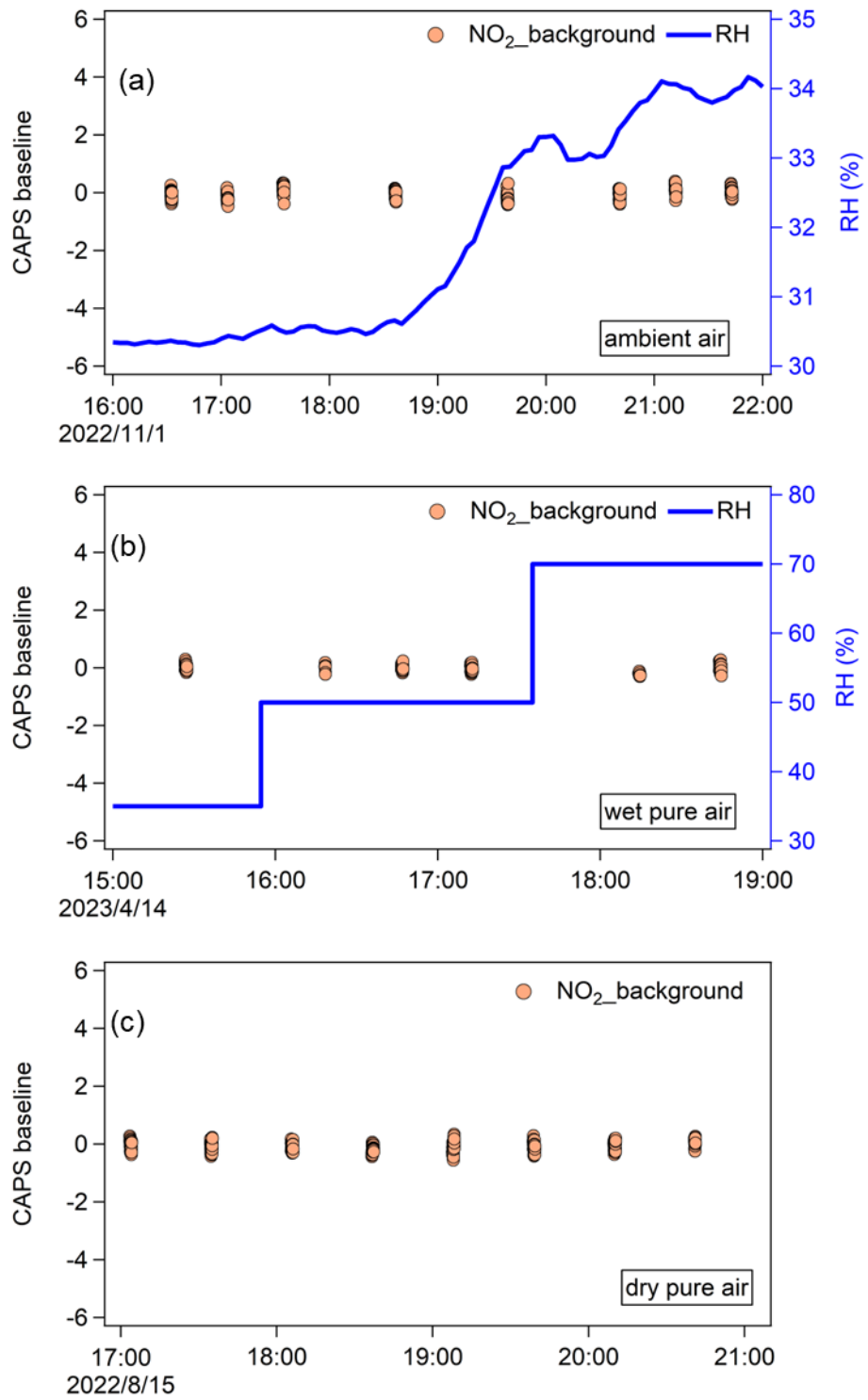
Figure S11. Time series of CAPS baseline and RH when measuring ambient air (a), and when injecting wet (b) and dry (c) pure air in the laboratory, respectively.
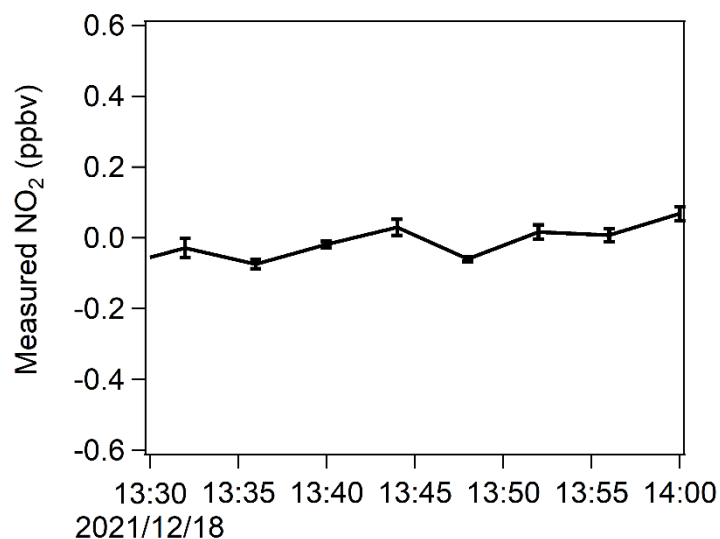
181

182 **1.5 The quantitative conversion efficiency of O_3 to NO_2 (α) in the NO-reaction chamber**

183
184 **Figure S12: Schematic diagram for measuring O_3 to NO_2 conversion efficiency in the NO-reaction chamber**
185 **(MFC: Mass Flow Controller).**

186
187 **Figure S13 Time series of NO_2 when injecting NO into CAPS-NO_2 monitor.**

188 **1.6 The airtightness of the reaction and reference chambers**

189
190
191 **Figure S14. Schematic diagram for investigating the airtightness of the reaction and reference chambers,**
192 **where MFC1 could measure air flow rate and pressure at the chamber inlet, MFC2 could measure air flow**
193 **rate and pressure at the chamber outlet.**

194

Table S8: Airtightness estimate of the reaction and reference chambers by testing the differences of (air flow rate × gas pressure) at the inlet and outlet of the reaction and reference chambers.

	Inlet flow rate (L min^{-1})	Inlet pressure (PSIA)	Inlet flow rate × Inlet pressure	Outlet flow rate (L min^{-1})	Outlet pressure (PSIA)	Outlet flow rate × Outlet pressure	Δ (Air flow rate × Pressure) (Difference at inlet and outlet)/ (Inlet flow rate × Inlet pressure) (%)
Reaction chamber	3.80	14.67	55.74	3.81	14.63	55.74	0.00
	3.46	13.48	46.64	3.51	13.43	47.14	1.07
	3.19	12.51	39.90	3.22	12.42	39.99	0.22
	2.93	11.54	33.81	3.00	11.53	34.59	2.33
Reference chamber	3.80	14.68	55.78	3.80	14.61	55.52	0.47
	3.33	13.04	43.42	3.38	13.00	43.94	1.20
	3.12	12.3	38.37	3.16	12.14	38.36	0.03
	2.83	11.25	31.84	2.91	11.24	32.71	2.73

S2: The LOD and measurement error of the NPOPR detection system.

Table S9. The upper limit values of LODs of the CAPS-NO$_2$ monitor for the reaction chamber, reference chamber, and $P(O_3)_{net}$ at different flow rates.

Flow rate of air (L min^{-1})	LOD (3σ)		
	Reaction chamber (ppbv)	Reference chamber (ppbv)	$P(O_3)_{net}$ (ppbv h^{-1})
1.3	0.02	0.02	0.07
3	0.10	0.10	1.4
5	0.13	0.07	2.3

The $P(O_3)_{net}$ error was calculated according the instrumental error of the CAPS-NO$_2$ monitor and the O$_3$ light-enhanced loss in the reaction and reference chambers. More details are described as follows:

Calibration of CAPS NO$_2$ monitor CAPS NO$_2$ monitor was used to measure the NO$_2$ standard gas after we have calibrated it using the gas-phase titration method using NO and O$_3$. We used the CAPS-NO$_2$ monitor reading as a transition value between the two to obtain the NO$_2$ standard gas and NO+O$_3$ mixing ratios corresponding to the same CAPS-NO$_2$ monitor reading. Results showed the purification of NO$_2$ standard gas was good enough to calibrate CAPS-NO$_2$ monitor, as shown in Fig. S15

y=(1.01±0.01)x
r²=1.05
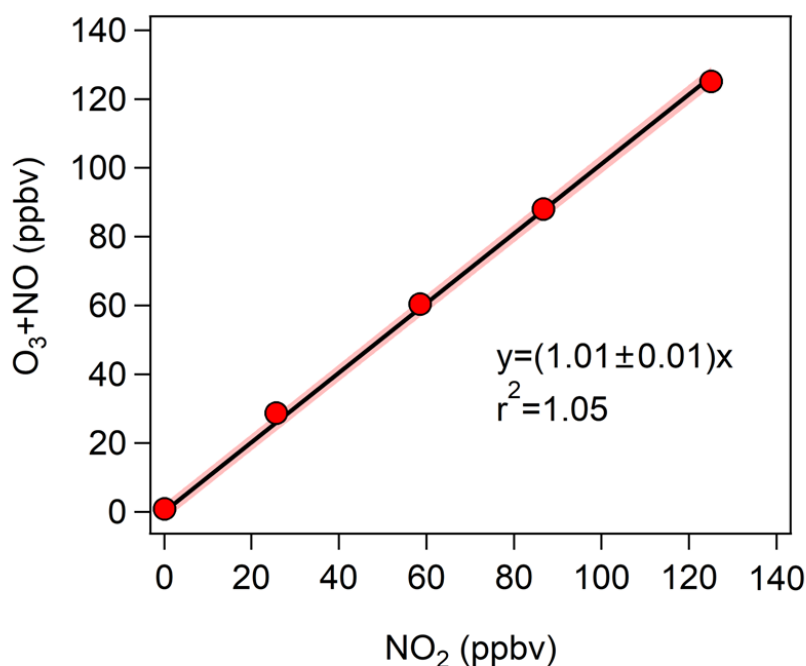
**Figure. S15 Correlation between NO₂ standard gas and the NO₂ generated using the gas-phase titration method (NO + O₃).**

The instrumental error of CAPS-NO₂ monitor $((O_{X_{CAPS}})_{error})$ was calculated from the fluctuation range of the 68.3 % confidence interval of the calibration curve as shown in Fig. 4, the relationship between the $(O_{X_{CAPS}})_{error}$ and the measured Ox value ($f_{measured}$) can be expressed as a power function curve, as shown in Eq. (S6):

$$(O_{X_{CAPS}})_{error} = 9.72 f_{measured}^{-1.0024} \tag{S6}$$

The light-enhanced loss of O₃ in the reaction and reference chambers at 5 L min⁻¹ (the ambient observation used flow rate in this study) were investigated by carrying out the following experiment: injecting the O₃ with a mixing ratio of about 130 ppbv generated by the O₃ generator (P/N 97-0067-02, Analytic Jena US, USA) to ensure that no photochemical O₃ was produced during the outdoor experiment. The $J(O^1D)$, T, RH, P, and O₃ mixing ratios at the inlet and outlet of the reaction and reference chambers were measured simultaneously. The T and RH were measured by the thermometer (Vaisala, HMP110, USA). The light-enhanced loss coefficient of O₃ (γ) was calculated using Eq. (S7), the relationship of $J(O^1D)$ with γ is shown in Fig. S16a. The obtained γ -$J(O^1D)$ equation listed in Eq. (S7) was used to correct the light-enhanced loss of O₃ in the reaction and reference chambers during the daytime to excluded the influence of light-enhanced loss.

19

227 $$\gamma = \frac{d[O_3] \times D}{\omega \times [O_3] \times \tau}$$ (S7)

228 where $d[O_3]$ represents the difference between the O_3 mixing ratios at the inlet and outlet of the reaction

229 and reference chambers, D is the diameter of the chambers, ω is the average velocity of O_3 molecules,

230 $[O_3]$ is the injected O_3 mixing ratio at the inlet of the reaction and reference chambers, and τ is the

231 average residence time of the air in the reaction and reference chambers.
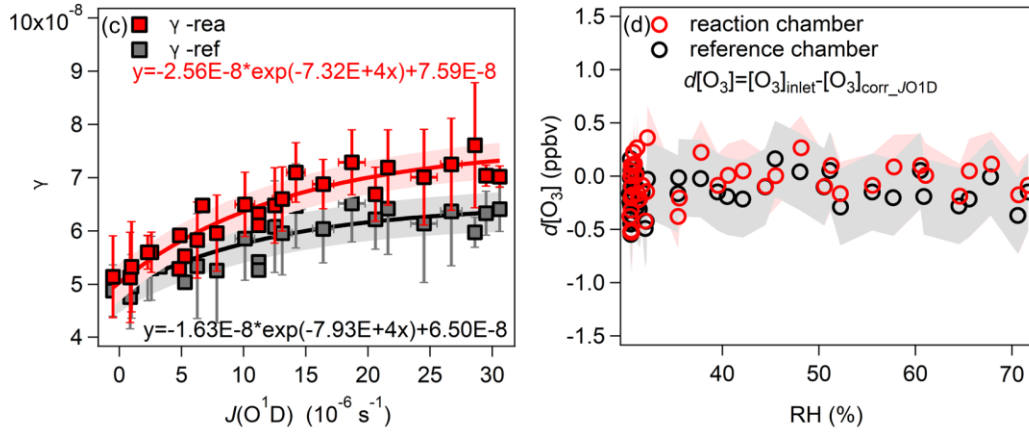
232

233 **Figure S16: The relationship of (a) γ and $J(O^1D)$ and (b) RH and $d[O_3]$ in the reaction and reference**
234 **chambers, which is calculated from the 68.3 % confidence interval of the fitting lines between γ and $J(O^1D)$,**
235 **the shaded areas represented the maximum fluctuation range under this confidence level.**

236 When quantifying the light-enhanced O_3 loss ($d[O_3]$) during ambient air measurement, we first

237 calculate γ using the measured $J(O^1D)$ and the γ-$J(O^1D)$ equations listed in Fig. S16a in the reaction

238 and reference chambers, then using the measured $[O_3]$ and Eq. (S7) to calculate $d[O_3]$.

239 The O_3 mixing ratio change after the correction of the light-enhanced loss of O_3 ($d[O_3]$) showed no

240 clear correlation with RH for both reaction and reference chambers, as shown in Fig. S16b, which

241 indicates that the RH had no influence to the O_3 mixing ratio change during the observation period. It

242 should be noted that the final error of Ox of the reaction and reference chambers includes the

243 measurement error of CAPS-NO_2 monitor (calculated by Eq. (S6)) and the error caused by γ, so the

244 measured $P(O_3)_{net}$ error can be calculated according to Eq. (7) in manuscript.

245 $$(O_X)_{error} = \sqrt{(O_{X\gamma})_{error}^2 + (O_{XCAPS})_{error}^2}$$ (S8)

246 where $(O_{X\gamma})_{error}$ represents the error of the Ox of the reaction and reference chambers corrected by γ.

247

S3: Supplement materials for the field observations.

Figure S17 shows the measurement site of the observation campaign, conducted at the Shenzhen Meteorological Gradient Tower (SZMGT), which is located in Shenzhen, Pearl River Delta (PRD) region in China.
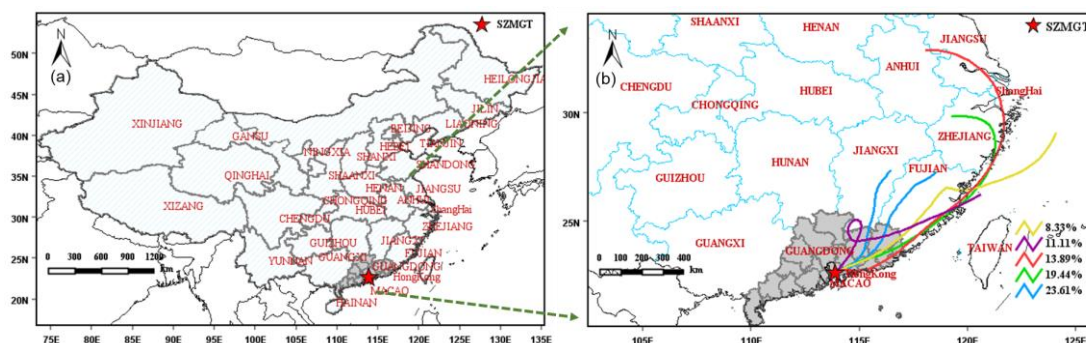
Figure S17: (a)The geographic location of the measurement site and (b) the integrated ambient air backward trajectories during sampling period from 7 December, 00:00 to 10 December 2021, 00:00 in Shenzhen (China). The above figures were obtained by using the MeteoInfo weather mapping software in the TrajStat plugin (Deshpande et al., 2016; Hao et al., 2020). Figure S17b was obtained by the Internet-based Hybrid-Single Particle Lagrangian Integrated Trajectory (HYSPLIT) Model, the required data was downloaded via ftp://arlftp.arlhq.noaa.gov/pub/archives/gdas1 (NOAA). Frequency grid resolution: 5.0° × 5.0°，trajectory duration: 72 h. The air mass during the campaign were mainly from Jiangxi and Fujian, which had a 23.61 % probability, followed by Zhejiang, Anhui, east coast, and East China Sea, which had 19.44 %, 13.89 %, 11.11 %, and 8.33 % probability, respectively.

281 **Table S10a: Summary of maximum $P(O_3)_{net}$ of field measurements in literatures.**

Measurement site	The type of site	Time	$P(O_3)_{net}$ (ppbv h^{-1})	Reference
Wakayama, Kyoto, Japan	remote area	27 July to 8 August 2014	10.5 ppbv h^{-1}	Sadanaga et al., 2017
State College, Pennsylvania, U.S.A.	urban area	Summer 2008	~30 ppbv h^{-1}	Cazorla et al., 2010
Houston, Texas, U.S.A.	urban area	October 2013	40-50 ppbv h^{-1}	Baier et al., 2015
Bloomington, Indiana, U.S.A.	a site 2.5 km northeast of the Indiana University Bloomington campus	30 May 2010	~30 ppbv h^{-1}	Sklaveniti et al., 2018
Houston, Texas, U.S.A.	urban area	15 April to 31 May 2009	100 ppbv h^{-1}	Ren et al., 2013
Shenzhen, Guangdong, China	a village in Bao'an district	7 to 9 December 2021	34.1 ppbv h^{-1}	This study

282

283 **Table S10b: Summary of maximum $P(O_3)_{net}$ of model simulation in literatures.**

284

Site	The type of site	Time	$P(O_3)_{net}$ (ppbv h^{-1})	Reference
Fukue Island, Japan	a remote area	May to June 2009	1-2 ppbv h^{-1}	Kanaya et al., 2016
Chelmsford, Essex, U.K.	a site 2 miles west of Chelmsford in Essex and 25 miles north east of London	Summer 2003	7.2 ppbv h^{-1}	Emmerson et al., 2007
Houston, Texas, U.S.A.	suburban area	the September 2013	~10 ppbv h^{-1}	Mazzuca et al., 2016
Houston, Texas, U.S.A.	urban area	from 15 April to 31 May 2009	15-20 ppbv h^{-1}	Ren et al., 2013
Houston, Texas, U.S.A.	urban area	from August to September 2006	45 ppbv h^{-1}	Chen et al., 2010; Chen et al., 2012
Houston, Texas, U.S.A.	urban area	September 2013	~30 ppbv h^{-1}	Mazzuca et al., 2016

285

286 **S4: Supplement materials for the MCM modeling.**

287 **Table S11. VOCs mixing ratios during 7- 9 December 2021 in SZMGT (units: pptv) used by the model.**

Chemicals	Classification	Mean±SD (pptv)	Chemicals	Classification	Mean±SD (pptv)
Alkanes		30516±27079	Aromatics		7098±5855
n-butane	NMHC	8803±6422	toluene	NMHC	3684±2688
propane	NMHC	7086±5169	*m/p*-xylene	NMHC	1392±1370
isobutane	NMHC	4983±3635	ethylbenzene	NMHC	591±582
ethane	NMHC	3461±2525	*o*-xylene	NMHC	572±563
isopentane	NMHC	1712±1249	benzene	NMHC	528±336
n-pentane	NMHC	1570±1146	styrene	NMHC	159±191
n-hexane	NMHC	633±462	1,2,4-trimethylbenzene	NMHC	39±29
2-methylpentane	NMHC	473±345	*m*-ethyltoluene	NMHC	38±28
3-methylpentane	NMHC	423±308	*p*-ethyltoluene	NMHC	21±15
3-methylhexane	NMHC	252±184	*n*-propylbenzene	NMHC	21±15
2-methylhexane	NMHC	195±142	*o*-ethyltoluene	NMHC	20±15
n-heptane	NMHC	178±130	isopropylbenzene	NMHC/	13±10
methylcyclopentane	NMHC	125±91	1,2,3-trimethylbenzene	NMHC	12±9
2,3-dimethylbutane	NMHC	122±89	1,3,5-trimethylbenzene	NMHC	7±5
n-octane	NMHC	109±80	OVOCs		40695±27180
methylcyclohexane	NMHC	102±74	formaldehyde	OVOCs	10558±5113
2,2-dimethylbutane	NMHC	71±52	ethanol	OVOCs	10537±7136
n-dodecane	NMHC	68±50	methanol	OVOCs	10320±6944
n-decane	NMHC	49±35	acetone	OVOCs	5701±4024
n-nonane	NMHC	47±34	hydroxyacetone	OVOCs	4542±3227
n-undecane	NMHC	41±30	acetaldehyde	OVOCs	3010±1939
Alkenes		2419±2086	methyl ethyl ketone	OVOCs	2714±2277
ethylene	NMHC	1493±1089	acrolein	OVOCs	605±244
propylene	NMHC	411±300	methyl vinyl ketone	OVOCs	185±101
isoprene	BVOCs	351±182	methacrylaldehyde	OVOCs	128±70
1-butene	NMHC	163±119	*m*-cresol	OVOCs	46±43
1-pentene	NMHC	29±21	phenol	OVOCs	26±26
1-hexene	NMHC	15±11			
trans-2-butene	NMHC	11±8			
cis-2-butene	NMHC	11±8			
trans-2-pentene	NMHC	5±3			
cis-2-pentene	NMHC	3±2			
Acetylene		1858±1356			
Acetylene	NMHC	1858±1356			

288 *NMHC: non-methane hydrocarbon, BVOCs: biogenic volatile organic compounds, OVOCs: oxygenated
289 volatile organic compounds.

4.1 J values used in the MCM model simulation

291   The J values obtained from two methods (labeled as method I and II) were used in the 3$^{\text{rd}}$-stage 4-

292   min simulation. The Tropospheric Ultraviolet and Visible (TUV) radiation model (version 5.3) (Lantz et

293   al., 1996; Madronich and Flocke, 1999) was used to provide a representative spectral actinic flux in these

294   two methods. The photolysis frequencies of each measured species used in TUV model ($J_{\text{value TUV}}$) were

295   calculated by numerical summation over wavelength (Calvert et al., 2002):

296    $J_{\text{value TUV}} = \int_a^b \delta_i \times \phi_i \times F_i \, \Delta\lambda_i$ (S9)

297   where a and b represent the range of the set wavelength, δ_i, ϕ_i, and F_i stand for the absorption cross

298   section, quantum yield, and spectral actinic flux of the species i, respectively. The spectral actinic flux

299   was obtained from the TUV model, detailed information of these two methods is described in Tables S12

300   and S13.

301   **Table S12. J values used in the model simulation in reaction and reference chambers.**

	J values used in the model simulation	
	Measured J values: $J(NO_2)$, $J(O^1D)$, $J(HONO)$, $J(H_2O_2)$, $J(NO_3\_M)$, $J(NO_3\_R)$, $J(HCHO\_M)$, $J(HCHO\_R)$	Unmeasured J values: $J(HNO_3)$, $J(CH_3CHO)$, $J(MACR)$, $J(MEK)$, $J(HOCH_2CHO)$, $J(C_2H_5CHO)$, $J(C_3H_7CHO)$, $J(C_4H_9CHO)$, etc.
Method I	$J_{\text{trans measured}} \times J_{\text{value measured}}$	$J_{\text{trans TUV}} \times J_{\text{NO2 measured}}/J_{\text{NO2 TUV}} \times J_{\text{value TUV}}$
Method II	$J_{\text{trans TUV}} \times J_{\text{value TUV}}$	$J_{\text{trans TUV}} \times J_{\text{NO2 measured}}/J_{\text{NO2 TUV}} \times J_{\text{value TUV}}$

302   *$J_{\text{value measured}}$ and $J_{\text{value TUV}}$ represent the measured and TUV modeled J values of different species, respectively.

303    $J_{\text{trans measured}}$ represents the measured transmittivities of each measured species in the reaction and reference chambers,

304   which are listed in Table S7; $J_{\text{trans TUV}}$ represents the transmittivities of each measured species used in TUV model

305   in the reaction and reference chambers, where the $J_{\text{trans TUV}}$ in the reaction chamber is regarded as 100 % $J_{\text{trans TUV}}$,

306   in the reference chamber is calculated as $\frac{J_{\text{TUV}390\text{-}790\,\text{nm}}}{J_{\text{TUV}290\text{-}790\,\text{nm}}}$, where $J_{\text{TUV}390\text{-}790\,\text{nm}}$ equals to the J value at the wavelength of 390–

307   790 nm, $J_{\text{TUV}290\text{-}790\text{nm}}$ quals to the J value at the wavelength of 290–790 nm, the detailed $J_{\text{trans TUV}}$ values of different

308   species are shown in Table S13; $J_{\text{NO2 measured}}$ and $J_{\text{NO2 TUV}}$ represent the measured and TUV modeled J_{NO2}.

309

310   **Table S13. The transmittivities of J values used in TUV model ($J_{\text{trans TUV}}$) described in Table S12.**

	Transmittivities							
	$J(NO_2)$	$J(O^1D)$	$J(HONO)$	$J(H_2O_2)$	$J(NO_3\_M)$	$J(NO_3\_R)$	$J(HCHO\_M)$	$J(HCHO\_R)$
Reaction chamber	1.00	1.00	1.00	1.00	1.00	1.00	1.00	1.00
Reference chamber	0.30	0.00	0.01	0.00	1.00	1.00	0.01	0.01

311 **4.2 The modeling results by using *J* values obtained from method II**

312   The variations in the radical mixing ratios (i.e., HO_2, OH, RO_2) and NO_3, NO, NO_2, and O_3 mixing

313 ratios obtained from method I and method II during the 3rd-stage 4-min model simulation are shown in

314 Fig. 8 and Fig. S18, respectively. The production and destruction reactions of HO_2, OH, RO_2, and NO_3

315 in the reaction and reference chambers obtained from methods I and II are shown in Fig. 9 and Fig. S19,

316 respectively, the production and destruction reactions of RO_X in the reaction and reference chambers

317 obtained from methods I and II are shown in Fig. S20, the detailed ROx production pathways of

318 NO_3+VOCs are shown in Fig. S21, and the final modeling results are shown in Fig. 10 and Fig. S22.

319   From Fig. S18, in the reaction chamber, HO_2, OH, RO_2, and NO_3 mixing ratios increased slightly

320 in the first few seconds and then became stable, their final concentrations were $1.97×10^8$, $7.61×10^6$,

321 $1.06×10^8$, and $8.36×10^6$ molecules cm^{-3}, respectively. In the reference chamber, HO_2, OH, and RO_2

322 concentrations declined in the 1st 20 seconds and then gradually became stable, their final concentrations

323 were $8.11×10^7$, $1.08×10^6$, and $5.68×10^7$ molecules cm^{-3}, respectively. On the contrary, the NO_3 mixing

324 ratio slightly increased at the 1st 1-2 min and then became stable at $1.88×10^7$ molecules cm^{-3}.
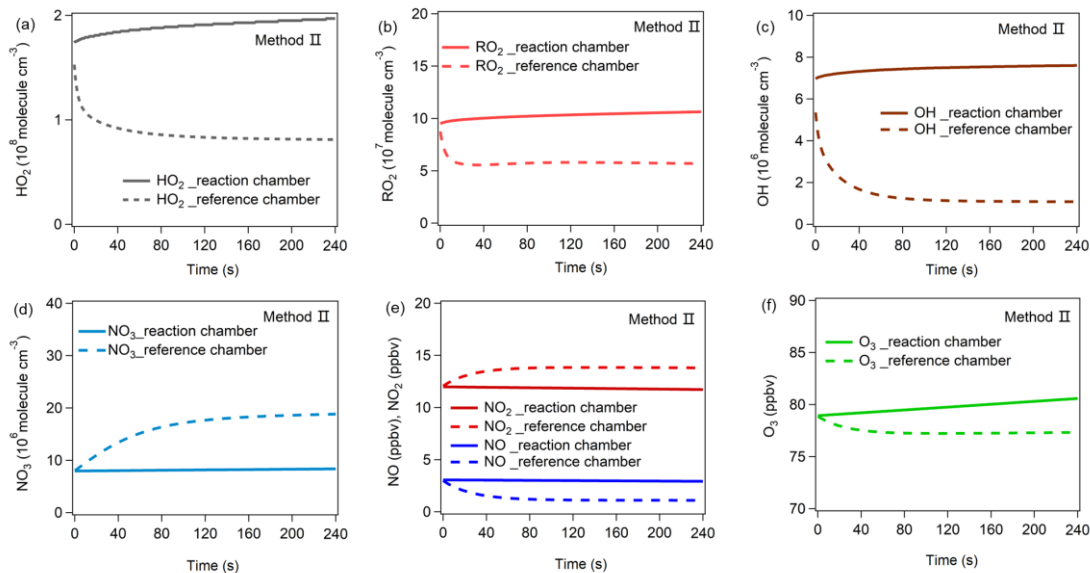
325

326 **Figure S18: The variations of (a) HO_2, (b) RO_2, (c) OH, (d) NO_3 and (e) NO, NO_2, and (f) O_3 mixing ratios**
327 **during the 3rd-stage 4-min model simulation using method II.**

328

329   OH, HO_2, RO_2, and NO_3 concentrations greatly impact the O_3 production and destruction rate. To

330 better understand the factors that drive the OH, HO_2, RO_2, and NO_3 concentration changes in method II,

331 we have added their production and destruction pathways in Fig. S19. We found that the decrease in HO_2

25

and RO_2 concentrations in the reference chamber in the 1st half minute was mainly due to NO titration effects, as high NO mixing ratios existed during the 1st half minute. The HO_2 and RO_2 concentrations were became stable afterwards, the main production pathway for HO_2 was $RO+O_2$ reaction/RO decomposition, followed by OH+VOCs reaction, OVOCs photolysis (i.e., $C_3H_4O_2$, $C_2H_2O_2$, $C_4H_6O_2$), and NO_3+VOCs reaction; while the main production pathway for RO_2 was OH+ VOCs reaction, followed by OVOCs photolysis (i.e., $C_3H_4O_2$, $C_2H_2O_2$, $C_4H_6O_2$), OH+CO, NO_3+VOCs reaction, etc.; the main destruction pathways for HO_2 and RO_2 were $HO2+NO$ and RO_2+NO, respectively. The main OH production and destruction pathways in the reference chamber was HO_2+NO reaction and OH+ VOCs reaction, respectively. Due to sufficiently high $J(NO_3)$ (~ 100 % of that in the reaction chamber) and NO_2 concentrations in the reference chamber, the NO_3 photolysis and NO_2+NO_3 reaction consumed NO_3 in the reference chamber, but the NO_3 concentrations were still high due to high production rates of NO_3 at the same time. Similar with the results obtained from method I as described in the main manuscript, for method II, the main NO_3 source in the reference chamber was the NO_2+O_3 reaction, followed by N_2O_5 decomposition. The NO concentrations were relatively high in the 1st minute and consumed NO_3 very quickly, but due to continuous NO_3 sources, the net NO_3 production rates ($P(NO_3)_{net}$) were positive (as shown in Fig. S19b4), which caused the NO_3 concentration to continue to increase (as shown in Fig. S18d). The main difference in NO_3 production in the reference chamber compared to that in the reaction chamber was the much higher N_2O_5 decomposition, which was mainly due to the high NO_2 concentrations in the reference chamber. On the other hand, although the $NO+NO_3$ reaction was also one of the dominant NO_3 destruction pathways, NO_3 consumed by the $NO+NO_3$ reaction was significantly smaller than NO_3 produced by the NO_2+O_3 reaction. The integrated production and destruction rates of ROx are shown in Fig. S20.
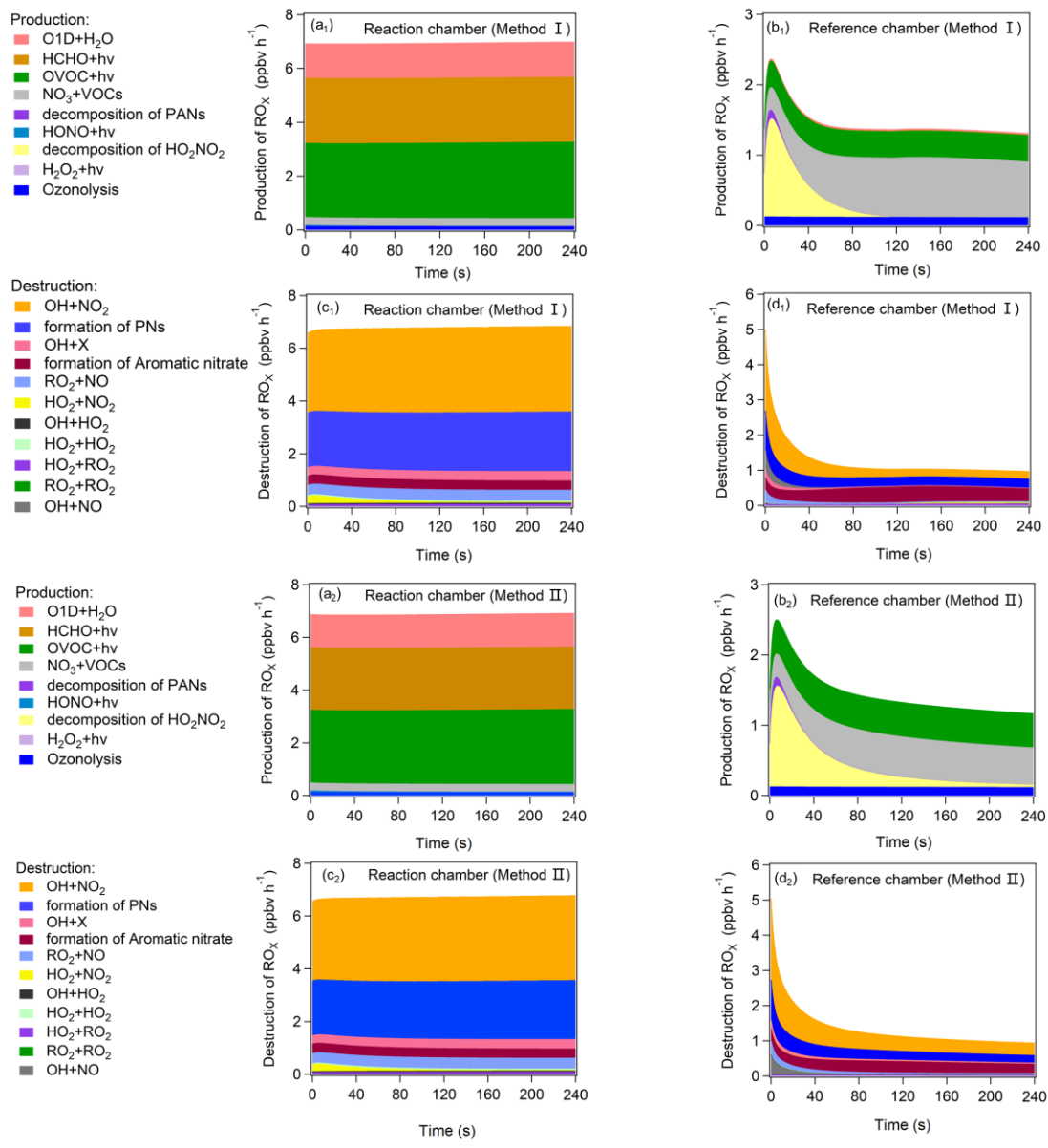
355
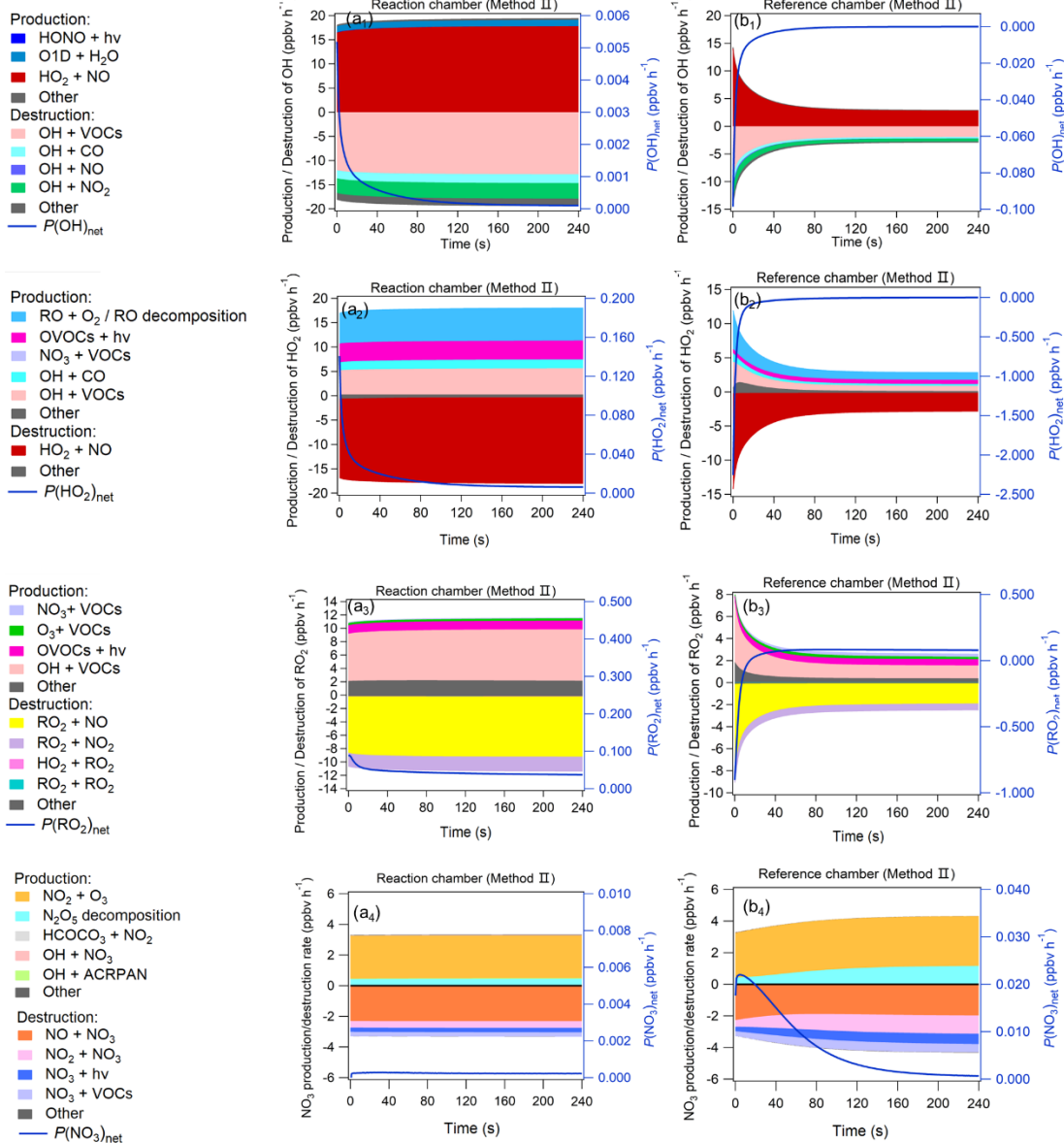
**Figure S19: Production and destruction pathways of OH(a1, b1), HO2(a2, b2), RO2(a3, b3), and NO3(a4, b4)**

during the 3rd-stag 4-min model simulation in the reaction and reference chambers in method II.

357

358

359

360 **Figure S20: Production and destruction pathways of RO_X during the 3rd-stage 4-min model simulation in the**

361 **reaction and reference chambers (PAN: Peroxyacetyl Nitrate; PNs: formations of all peroxynitrate (including**

362 **$CH_3O_2NO_2$ and PAN; X: PAN and the net loss of OH+NO to form HONO (usually small)).**

363

364
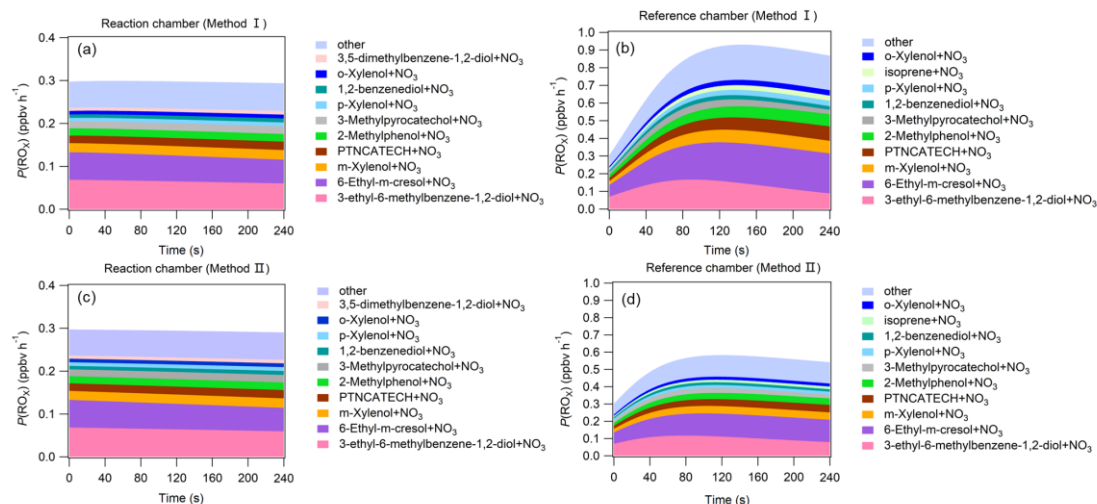
Figure S21: The _P_(ROx) pathways related to NO₃+VOCs reactions during the 3ʳᵈ-stage 4-minute model simulation in the reaction and reference chambers in method I (a)-(b) and method II (c)-(d).

Figures S22a–d show the modeled $P(O_3)_{net}$ and the source and sink of various species during the 3ʳᵈ-stage 4-min simulation in method II. Figure S22a shows the steady state of $P(O_3)_{net}$ and the various species in the ambient atmosphere achieved in the last 1 s of the 2ⁿᵈ-stage simulation; Figs. S22b-c show the modeled $P(O_3)_{net}$ and the O₃ chemical budgets in the reaction and reference chambers during the model simulation period; Figure S22d summarized the modeled $P(O_3)_{net}$ in the ambient atmosphere, and that in the reaction and reference chambers, in order to compare the modeled results with our measurement results, we calculated the integral mean of the modeled $P(O_3)_{net}$ in the reaction and reference chambers and appended the related measured $P(O_3)_{net}$ value during this 4-min simulation time onto Fig. S22d. Further, the reaction weights of different production and destruction reactions process of O₃ are shown in Figs. S22e–h.
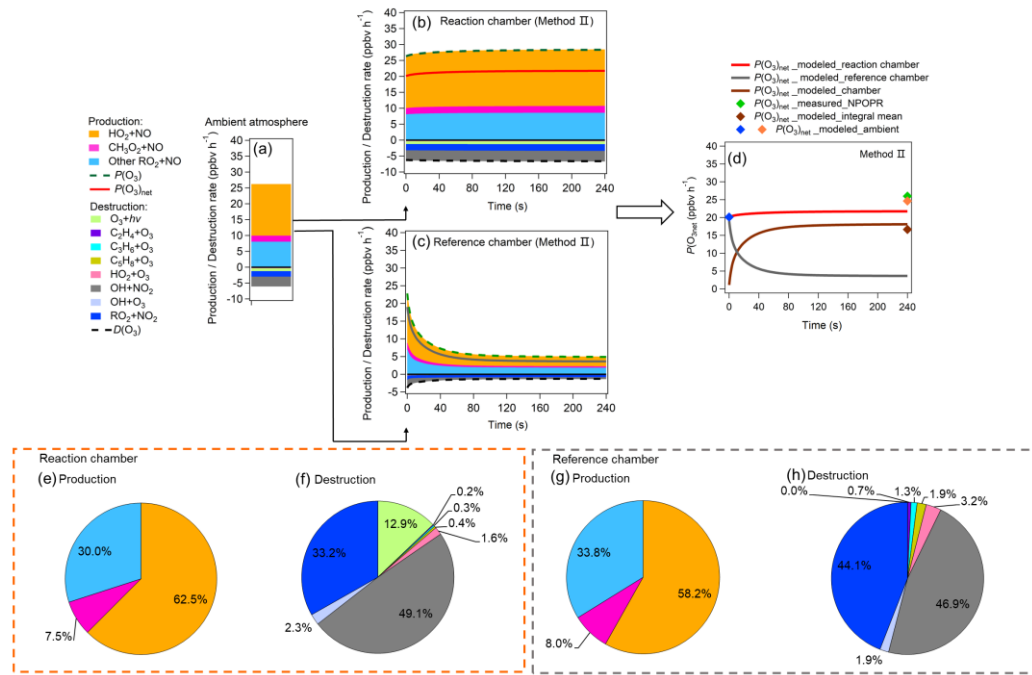
Figure S22: (a)–(c) Modeled $P(O_3)_{net}$ and O_3 chemical budgets in (a) the ambient air when injected into the reaction and reference chambers and (b–c) the reaction and reference chambers during the 4-min model simulation; (d) $P(O_3)_{net}$, where $P(O_3)_{net\_modeled\_ambient}$ represent the modeled $P(O_3)_{net}$ in ambient air at the time before (blue marker) and after (orange marker) the sampled ambient air was injected into the dual-channel reaction chamber. $P(O_3)_{net\_modeled\_reaction\ chamber}$ and $P(O_3)_{net\_modeled\_reference\ chamber}$ represent the $P(O_3)_{net}$ change trends during the 4-min photochemical reactions in the reaction and reference chambers, respectively. $P(O_3)_{net\_modeled\_chamber}$ = $P(O_3)_{net\_modeled\_reaction\ chamber}$–$P(O_3)_{net\_modeled\_reference\ chamber}$, and $P(O_3)_{net\_modeled\_integral\ mean}$ represents the integral mean of the $P(O_3)_{net\_modeled\_chamber}$. Moreover, $P(O_3)_{net\_measured\_NPOPR}$ is the $P(O_3)_{net}$ measured by NPOPR detection system. (e)–(h) Reaction weights of each production and destruction reaction process of O_3 in the reaction and reference chambers in method II.
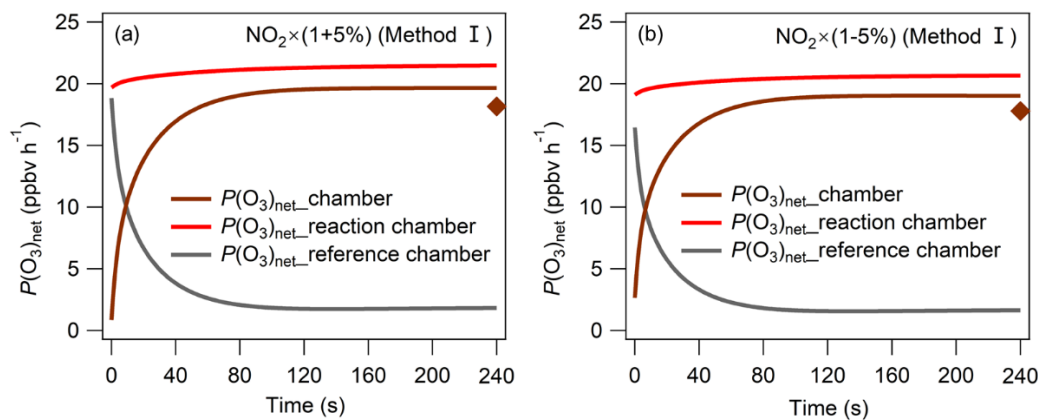
Figure S23: $P(O_3)_{net}$ changing in the reaction and reference chambers in method I with ± 5 % of measured NO_2.

395
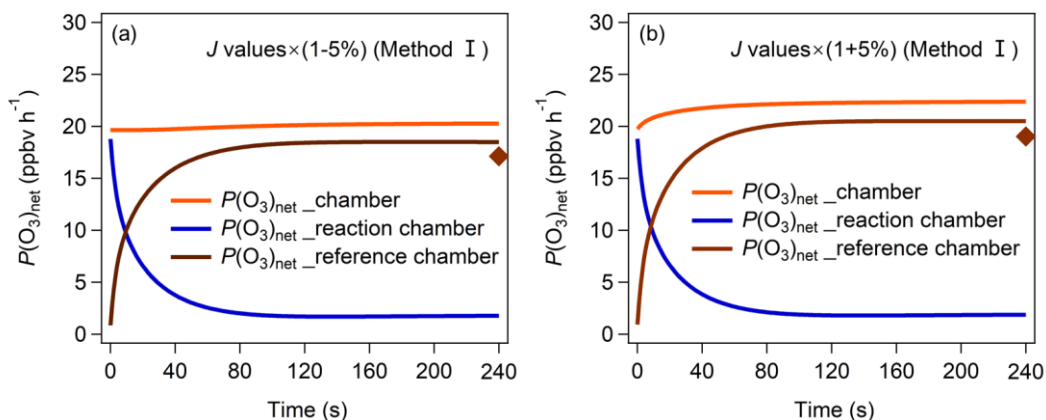
Figure S24: $P(O_3)_{net}$ changing in the reaction and reference chambers in method I with ± 5 % of measured J values.

From Fig. S22, the $P(O_3)$ and $D(O_3)$ were almost the same within the 4-min reaction in the reaction chamber (all species reached a steady state condition), while the $P(O_3)$ and $D(O_3)$ in the reference chamber decreased significantly within the 1st minute, and kept stable in the following minutes. In the reaction chamber, the HO_2+NO reaction contributed most to $P(O_3)$, accounting for 62.5 % of the total $P(O_3)$, with the integral mean value of 17.5 ppbv h^{-1} in the reaction chamber. The second important pathway of $P(O_3)$ was RO_2+NO (occupied 37.5 % of the total $P(O_3)$). The reaction of RO_2+NO contained more than 1200 types of RO_2 radicals, and the pathway of CH_3O_2+NO contributed 7.5 % of the total $P(O_3)$. The most important contributor of $D(O_3)$ was $OH+NO_2$ (49.1 %), followed by RO_2+NO_2 (33.2 %), O_3 photolysis (12.9 %), O_3+OH (2.3 %), O_3+HO_2 (1.6 %), $C_5H_8+O_3$ (0.4 %), $C_3H_6+O_3$ (0.3 %), and $C_2H_4+O_3$ (0.2 %). In the reference chamber, the integral mean value of $P(O_3)$ was 3.7 ppbv h^{-1}, the HO_2+NO contributed most to $P(O_3)$ (accounting for 58.2 % of the total $P(O_3)$), followed by RO_2+NO (occupied 41.8 % of the total $P(O_3)$), in which the CH_3O_2+NO contributed 8.0 % of the total $P(O_3)$. The most important contributor of $D(O_3)$ was $OH+NO_2$ (46.9 %), followed by RO_2+NO_2 (44.1 %), O_3+HO_2 (3.2 %), $C_5H_8+O_3$ (1.9 %), O_3+OH (1.9 %), $C_3H_6+O_3$ (1.3 %), $C_2H_4+O_3$ (0.7 %), and O_3 photolysis (0.0 %). For all $P(O_3)$ reactions, the weight of RO_2+NO reaction in the reference chamber was 4.3 % higher than that in the reaction chamber, however, for all $D(O_3)$ reactions, the weight of RO_2+NO_2 reaction in the reference chamber was 10.9 % higher than that in the reaction chamber, which will somehow mitigate the high $P(O_3)$ caused by RO_2+NO in the reference chamber. Figure S22d shows that the $P(O_3)_{net}$ (26.0 ppbv h^{-1}) measured by the NPOPR detection system was 9.3 ppbv h^{-1} higher than the modeled value (16.7 ppbv h^{-1}). This difference was much larger than 7.5 ppbv h^{-1} obtained from method

418 I, this may be due to the transmittance of $J(NO_2)$ in the reference chamber in method II ($\sim$ 30 %) was

419 much higher than that in method I ($\sim$ 9 %), NO_2 photolysis products NO, it involved in the main O_3

420 production reactions HO_2+NO and RO_2+NO, so the modeled $P(O_3)_{net}$ in the reference chamber was

421 slightly overestimated in method II, thus leading to an underestimation of total $P(O_3)_{net}$.

422

References

Baier, B. C., Brune, W. H., Lefer, B. L., Miller, D. O., and Martins, D. K.: Direct ozone production rate measurements and their use in assessing ozone source and receptor regions for Houston in 2013, Atmos. Environ., 114, 83-91, http://dx.doi.org/10.1016/j.atmosenv.2015.05.033, 2015.

Calvert, J.G., Atkinson, R., Becker, K.H., Kamens, R.M., Seinfeld, J.H., Wallington, T.H., Yarwood, G.: The mechanisms of atmospheric oxidation of the aromatic hydrocarbons, Oxford University Press, 2002.

Cazorla, M., and Brune, W. H.: Measurement of ozone production sensor, Atmos. Meas. Tech., 3, 545-555, https://doi.org/10.5194/amt-3-545-2010, 2010.

Chen, S., Ren, X., Mao, J., Chen, Z., Brune, W. H., Lefer, B., Rappenglück, B., Flynn, J., Olson, J., and Crawford, J. H.: A comparison of chemical mechanisms based on TRAMP-2006 field data, Atmos. Environ., 44, 4116-4125, https://doi.org/10.1016/j.atmosenv.2009.05.027, 2010.

Chen, S., and Brune, W. H.: Global sensitivity analysis of ozone production and O_3-NO_X-VOC limitation based on field data, Atmos. Environ., 55, 288-296, https://doi.org/10.1016/j.atmosenv.2012.03.061, 2012.

Deshpande, R. D., Medha, D., Virendra, P., Kumar, H., & Gupta, S. K. : Water vapor source identiffcation for daily rain events at Ahmedabad in semi-arid western India: Wind trajectory analyses. Meteorological Applications, 22, 754–762. https://doi.org/10.1002/met.1515, 2016.

Emmerson. K. M., Carslaw. N. C., Carslaw. D. C., Lee. J. D., McFiggans. G., Bloss. W. J., Gravestock. T., Heard. D. E., Hopkins. J., Ingham. T., Pilling. M. J., Smith. S. C., Jacob. M., and Monks. P. S.: Free radical modelling studies during the UK TORCH Campaign in Summer 2003, Atmos. Chem. Phys., 7, 167–181, https://doi.org/10.5194/acp-7-167-2007, 2007.

Hao, C., Song, L., and Zhao, W.: HYSPLIT-based demarcation of regions affected by water vapors from the South China Sea and the Bay of Bengal, European Journal of Remote Sensing, 54, 348-355, https://doi.org/10.1080/22797254.2020.1795730, 2020.

Kanaya, Y., Tanimoto, H., Yokouchi, Y., Fumikazu Taketani, F. T., Komazaki, Y., Irie, H., Takashima, H., Pan, X., Nozoe, S., and Inomata, S.: Diagnosis of photochemical ozone production rates and limiting factors in continental outflow air masses reaching Fukue Island, Japan: ozone-control implications, Aerosol. Air. Qual. Res., 16, 430-441, https://doi.org/10.4209/aaqr.2015.04.0220, 2016.

452 Lantz, K.O., Shetter, R.E., Cantrell, C.A., Flocke, S.J., Calvert, J.G., Madronich, S.: Theoretical,

453   actinometric, and radiometric determinations of the photolysis rate coefficient of NO2 during the

454   Mauna Loa Observatory Photochemistry Experiment 2, J. Geophys. Res.-Atmos., 101, 14613-14630,

455   https://doi.org/10.1029/96JD00215,1996.

456 Madronich, S. and Flocke, S. (ed. by P. Boule): The role of solar radiation in atmospheric chemistry, 2,

457   Environmental photochemistry, 1-26, 1999.

458 Mazzuca, G. M., Ren, X., Loughner, C. P., Estes, M., Crawford, J. H., Pickering, K. E., Weinheimer, A.

459   J., and Dickerson, R. R.: Ozone production and its sensitivity to NOx and VOCs: results from the

460   DISCOVER-AQ field experiment, Houston 2013, Atmos. Chem. Phys., 16, 14463-14474,

461   https://doi.org/10.5194/acp-16-14463-2016, 2016.

462 Ren, X., van Duin, D., Cazorla, M., Chen, S., Mao, J., Zhang, L., Brune, W. H., Flynn, J. H., Grossberg,

463   N., Lefer, B. L., Rappenglück, B., Wong, K. W., Tsai, C., Stutz, J., Dibb, J. E., Thomas Jobson, B.,

464   Luke, W. T., and Kelley, P.: Atmospheric oxidation chemistry and ozone production: Results from

465   SHARP   2009   in   Houston,   Texas,   J.   Geophys.   Res.-Atmos.,   118,   5770-5780,

466   https://doi.org/10.1002/jgrd.50342, 2013.

467 Sadanaga, Y., Kawasaki, S., Tanaka, Y., Kajii, Y., and Bandow, H.: New system for measuring the

468   photochemical ozone production rate in the atmosphere, Environ. Sci. Technol., 51, 2871-2878,

469   https://doi.org/10.1021/acs.est.6b04639, 2017.

470 Sklaveniti, S., Locoge, N., Stevens, P. S., Wood, E., Kundu, S., and Dusanter, S.: Development of an

471   instrument for direct ozone production rate measurements: measurement reliability and current

472   limitations, Atmos. Meas. Tech., 11, 741-761, https://doi.org/10.5194/amt-11-741-2018, 2018.